

Quasiparticle Model of Quark-Gluon Plasma at Imaginary Chemical Potential

M. Bluhm¹ and B. Kämpfer^{1,2}

¹*Forschungszentrum Dresden-Rossendorf,
PF 510119, 01314 Dresden, Germany*

²*Institut für Theoretische Physik, TU Dresden, 01062 Dresden, Germany*

(Dated: February 2, 2008)

Abstract

A quasiparticle model of the quark-gluon plasma is compared with lattice QCD data for purely imaginary chemical potential. Net quark number density, susceptibility as well as the deconfinement border line in the phase diagram of strongly interacting matter are investigated. In addition, the impact of baryo-chemical potential dependent quasiparticle masses is discussed. This accomplishes a direct test of the model for non-zero baryon density. The found results are compared with lattice QCD data for real chemical potential by means of analytic continuation and with a different (independent) set of lattice QCD data at zero chemical potential.

PACS numbers: 12.38.Mh;12.39.-x

Keywords: quasiparticle model, imaginary chemical potential

I. INTRODUCTION

Strongly interacting matter, as described by QCD, exhibits an astonishingly rich phase structure. In the region of not too large baryon densities, the deconfinement transition from hadronic matter to a plasma built of quark-gluon constituents is the most prominent feature. It is signalled by a rapid change in the expectation value of the Polyakov loop and the chiral condensate where one assigns a pseudo-critical temperature T_c to this transition (cf. reviews, e. g. [1]). At higher temperatures, $T > 3T_c$, further structural changes are conjectured [2]. For non-zero quark chemical potential μ , corresponding to a finite net baryon density, many researchers argue on the change of the deconfinement border line, representing an analytic crossover, into a first-order transition curve. The onset of this sequence of first-order transitions is marked by a critical point being of second order which has attracted much attention recently (see [3]). The interest in this part of the phase diagram is triggered by the possibility to probe it under laboratory conditions in relativistic heavy-ion collisions.

With the advance of precision data from ultrarelativistic heavy-ion collisions at RHIC, the paradigm on the quark-gluon plasma has changed [4]: The notion of a strongly coupled plasma has been put forward to explain the seemingly very small viscosity to entropy ratio deduced from hydrodynamical fits to experimental data as in [5], and various models have been developed [6] to account for such a property. On the other hand, we are witnessing a vast progress in first principle calculations of thermodynamic properties of hot deconfined strongly interacting matter based directly on QCD [7–9]. While various observables such as pressure, energy density or numerous susceptibilities are addressed, the available lattice QCD data are obtained for different numerical set-ups, lattice sizes, flavor numbers and quark masses as well. Particular attempts are needed to access non-zero baryon densities because the notorious sign problem of the fermion determinant prevents a direct application of methods useful for zero baryon density. Nevertheless, a few methods have been developed to access non-zero baryon densities. Among such methods is the calculation of thermodynamic quantities at purely imaginary chemical potential. Here, the sign problem is avoided but the results have to be analytically continued to real chemical potential. In this respect it is useful to have a model at our disposal which is successfully probed for both, real and imaginary chemical potential, in order to accomplish the translation of results from imaginary to real chemical potential.

While baryon density effects are small for heavy-ion collisions at top-RHIC energies and will be even smaller for LHC energies, at least in the mid-rapidity region, for CERN-SPS and upcoming FAIR energies they are sizeable. In this respect, a firm knowledge of thermodynamic bulk properties of strongly interacting matter is highly desirable. As a step towards achieving this goal we are going to extend our quasiparticle model [10–13] to imaginary chemical potential. Here, information is obtained for $\mu^2 < 0$ allowing, in principle, for identifying $\mu = \pm i\mu_i$. The model has been tested successfully for real chemical potential [14], say in describing the Taylor expansion coefficients of the pressure as a series in powers of μ/T . In such a way, Peshier’s flow equation [11] is tested in some detail. This flow equation transports information about the effective coupling, G^2 , from the temperature axis to non-zero μ and determines to a large extent the dependence on μ and thus on baryon density. Another important piece of the model is the quasiparticle ansatz for dynamically generated effective masses of quarks $\propto (T^2 + \frac{\mu^2}{\pi^2})G^2$. When going to purely imaginary chemical potential $\mu \rightarrow \pm i\mu$ the sign of the μ^2 term is flipped, as also signs in Peshier’s flow equation are changed. Therefore, the μ dependence of the model is directly tested by considering an imaginary chemical potential.

In the following, two symmetries of the QCD partition function $Z(T, \mu)$ are of relevance: (i) $Z(T, \mu) = Z(T, -\mu)$, and (ii) $Z(T, i\mu_i) = Z(T, i(\mu_i + \frac{2\pi}{3}T))$, i. e. $Z(T, \mu)$ is periodic in μ_i with period $2\pi T/3$ [15]. Symmetry (i) makes Z an even function of μ (meaning that in a Taylor series expansion only even powers of μ/T , and thus also of μ_i/T , are encountered) such that we can focus on $\mu = +i\mu_i$ only, while (ii) implies the Roberge-Weiss periodicity [15] which is anchored in the center symmetry. This periodicity is characterized by lines of first-order transitions (Z_3 transitions) at $\mu_i = \frac{\pi}{3}T(1 + 2k)$ for all integers k and sufficiently high temperature T while for smaller temperatures the behavior of thermodynamic quantities is analytic. The endpoint of first-order transitions, T^E , is determined by the crossing of the Roberge-Weiss transition line with the chiral critical line which is also a first-order transition line for $N_f = 4$ degenerate quark flavors [16]. The Roberge-Weiss periodicity implies that in the $T - \mu_i/T$ plane all sectors between $\mu_i/T = \frac{2\pi}{3}k$ and $\mu_i/T = \frac{2\pi}{3}(k + 1)$ are copies of the sector between $\mu_i/T = 0$ and $\mu_i/T = \frac{2\pi}{3}$. Furthermore, the subsector between $\mu_i/T = \pi/3$ and $\mu_i/T = 2\pi/3$ is an reflected copy of the subsector between $\mu_i/T = 0$ and $\mu_i/T = \pi/3$ mirrored at the first Roberge-Weiss transition line. As thermodynamic quantities behave non-analytically at $\mu_i/T = \pi/3$ (Roberge-Weiss transition), an analytic continuation of

results obtained for imaginary chemical potential to real μ has direct access to the region $\mu < \pi/3 T$ only.

Due to the severe approximations made when linking our phenomenological model [10, 11, 13] to QCD [12], the Roberge-Weiss periodicity is not longer apparent. Having this in mind, we translate the model to imaginary chemical potential in section II. The comparison with lattice QCD data at imaginary chemical potential is performed in section III, where also the continuation to real chemical potential is presented. This allows, in addition, for a comparison with another and independent set of lattice QCD data obtained at $\mu = 0$ (section IV). Furthermore, we investigate in detail the impact of the baryo-chemical potential dependence of the quasihquark and quasihgluon masses (selfenergies) on the found results and discuss the deconfinement border line in the phase diagram of strongly interacting matter. Our results are summarized in section V. Appendices A and B contain Peshier's flow equation for imaginary chemical potential and a discussion about the parametrization of the μ dependence of the density.

II. QUASIPARTICLE MODEL AT IMAGINARY CHEMICAL POTENTIAL

The employed model is based on a two-loop Φ functional approach to QCD with corresponding one-loop self-energies considered in HTL approximation in the asymptotic limit and the neglect of finite width effects, (anti)plasmino and longitudinal gluon contributions as well as Landau damping [12]. The QCD running coupling is replaced by an effective coupling $G^2(T, \mu)$ which is subject to Peshier's flow equation [11] resting on a thermodynamic self-consistency condition and the stationarity of the grand canonical potential $\Omega = -pV = -T \ln Z$, where p denotes the pressure and V the volume of the system. Straightforward replacement of $\mu = i\mu_i$ in $p(T, \mu)$ renders the net quark number density, $n(T, i\mu_i) = -i\partial p(T, i\mu_i)/\partial \mu_i$, related to the net baryon density $n_B = \frac{1}{3}n$, to

$$n(T, i\mu_i) = \frac{d_q}{2\pi^2} \int_0^\infty dk k^2 \left(\frac{1}{e^{(\omega_q - i\mu_i)/T} + 1} - \frac{1}{e^{(\omega_q + i\mu_i)/T} + 1} \right) \quad (1)$$

$$= i \frac{d_q}{\pi^2} \int_0^\infty dk k^2 \left(\frac{e^{\omega_q/T} \sin(\mu_i/T)}{e^{2\omega_q/T} + 2e^{\omega_q/T} \cos(\mu_i/T) + 1} \right), \quad (2)$$

where $d_q = 2N_c N_f$ is the degeneracy factor of quarks for $N_c = 3$ colors and N_f quark flavors. The found result for n is purely imaginary and positive (negative) for small positive (negative) μ_i , i. e. n is an odd function in μ_i .

The quark dispersion relation $\omega_q(k)$ employed in Eqs. (1, 2) reads

$$\omega_q^2 = k^2 + M_\infty^2 \quad (3)$$

with asymptotic mass $M_\infty^2 = m_q^2 + 2M_+^2$ using

$$M_+^2 = \frac{N_c^2 - 1}{16N_c} \left(T^2 - \frac{\mu_i^2}{\pi^2} \right) G^2(T, i\mu_i) \quad (4)$$

as plasma frequency. This dispersion relation is based on a calculation of one-loop self-energies with finite quark masses m_q in Feynman gauge in the asymptotic limit [17] for small m_q/T , where m_q may be temperature dependent as well to allow for a direct comparison with lattice QCD data. (A different approximation of M_∞ is discussed in section III C.) Eqs. (1, 2) highlight the quasiparticle character of the model: the baryon charge is carried by excitations with dispersion relation given by Eq. (3). The dependence of M_∞ on the chemical potential (cf. [18]) will be discussed in section III D.

Peshier's flow equation [11] for imaginary chemical potential reads

$$b = a_T \frac{\partial G^2}{\partial T} + a_{\mu_i} \frac{\partial G^2}{\partial \mu_i}, \quad (5)$$

where the coefficients b , a_T and a_{μ_i} depending on T , μ_i and $G^2(T, i\mu_i)$ are relegated to Appendix A. Transforming Eq. (5) to a system of three coupled ordinary differential equations, it can be solved by the methods of characteristics knowing, for instance, $G^2(T, \mu = 0)$. A convenient parameterization of $G^2(T, \mu = 0)$ is [11]

$$G^2(T \geq T_c, \mu = 0) = \frac{16\pi^2}{\beta_0 \log \xi^2}, \quad (6)$$

making some contact to perturbative QCD at very large temperatures. Here, $\beta_0 = \frac{1}{3}(11N_c - 2N_f)$ and ξ is parametrized phenomenologically as $\xi = \lambda(T - T_s)/T_c$ with scale parameter λ and T_s shifting the infrared divergence to $T = T_s + T_c/\lambda < T_c$ for appropriate parameters, while we focus here on the region $T \geq T_c$.

Results obtained for $\mu^2 < 0$ need to be analytically continued into the $\mu^2 > 0$ half-plane in order to achieve physical results. An effective analytic continuation requires a positive second derivative of Z with respect to μ , cf. [19, 20], i. e. the quark number susceptibility

$\chi(T, \mu) = \partial n(T, \mu) / \partial \mu > 0$. The QPM result for χ reads for imaginary chemical potential

$$\begin{aligned} \chi(T, i\mu_i) = & \frac{d_q}{2\pi^2 T} \int_0^\infty dk k^2 \frac{(2e^{3\omega_q/T} \cos(\mu_i/T) + 4e^{2\omega_q/T} + 2e^{\omega_q/T} \cos(\mu_i/T))}{(e^{2\omega_q/T} + 2e^{\omega_q/T} \cos(\mu_i/T) + 1)^2} \\ & + \frac{d_q}{2\pi^2 T} \int_0^\infty dk \frac{k^2}{\omega_q} \frac{(e^{3\omega_q/T} \sin(\mu_i/T) - e^{\omega_q/T} \sin(\mu_i/T))}{(e^{2\omega_q/T} + 2e^{\omega_q/T} \cos(\mu_i/T) + 1)^2} \\ & \times \frac{N_c^2 - 1}{8N_c} \left(\frac{2}{\pi^2} \mu_i G^2 - \left[T^2 - \frac{\mu_i^2}{\pi^2} \right] \frac{\partial G^2}{\partial \mu_i} \right); \end{aligned} \quad (7)$$

it is purely real and symmetric under $\mu_i \rightarrow -\mu_i$ (cf. Appendix A). Furthermore, for small μ_i , the first term in Eq. (7) is positive and dominates the second term. At $\mu = 0$, one finds

$$\chi(T, \mu = 0) = \frac{d_q}{\pi^2 T} \int_0^\infty dk k^2 \frac{e^{\tilde{\omega}_q/T}}{e^{2\tilde{\omega}_q/T} + 2e^{\tilde{\omega}_q/T} + 1} > 0, \quad (8)$$

where $\tilde{\omega}_q = \omega_q(T, \mu = 0)$.

III. COMPARISON WITH LATTICE QCD RESULTS FOR IMAGINARY MU

A. Baryon density and quark number susceptibility

We confront now the above introduced quasiparticle model (QPM) with lattice QCD data [19, 21] at non-zero T and μ_i obtained for $N_f = 4$ degenerate quark flavors with $m_q = 0.2T$; these calculations [19, 21] are performed on a lattice with temporal and spatial extensions $N_\tau = 4$ and $N_\sigma = 16$. Valuable information in such simulations with imaginary chemical potential is obtained for $\mu_i < 0$ [22] implying a negative imaginary part of the net quark number density $n(T, i\mu_i)$ according to Eq. (2). In the following, however, we will consider $\mu_i > 0$ which renders the sign of $n(T, i\mu_i)$ and accordingly the behavior of $\chi = \partial n / \partial (i\mu_i)$. Our model is formulated for a system infinite in space and time. Thus, we need a proper extrapolation of the lattice QCD data to the continuum limit ($N_\tau \rightarrow \infty$ at fixed temperature). Different estimates for a continuum extrapolation are conceivable. For instance, one may select a scaling factor strictly valid only for asymptotically high temperatures, or one may use as scaling factor the ratio of thermodynamic quantities for a massless, non-interacting gas of quarks and gluons known in the continuum limit and from lattice QCD for finite N_τ . Even though such estimates for a correction factor could depend on T , in general, we apply the latter procedure, assuming that the continuum extrapolations for QCD and for the non-interacting gas of quarks and gluons are similar (cf. discussion in

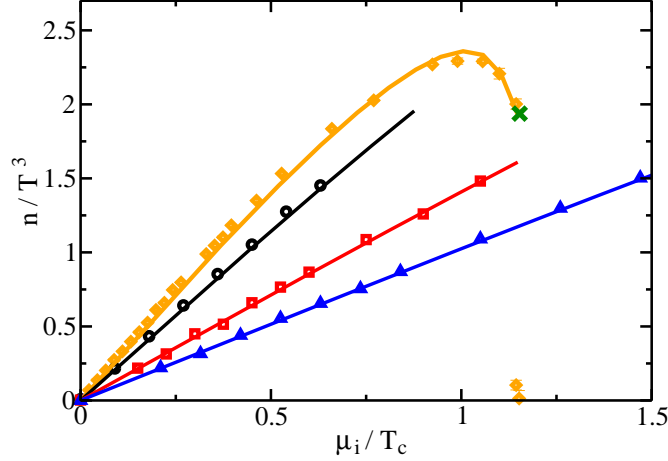


FIG. 1: Comparison of the QPM (solid curves) for the scaled net quark number density n/T^3 as a function of μ_i/T_c with continuum estimates of the lattice QCD data [19, 21] for temperatures $T = 1.1, 1.5, 2.5, 3.5 T_c$ (diamonds, circles, squares and triangles, respectively). The fat cross depicts the Roberge-Weiss critical chemical potential $\mu_c/T = \pi/3$ for $T = 1.1 T_c$, where we stopped our calculations.

[23] for pure SU(3) theory). In principle, however, a profound extrapolation to the continuum limit should be based on simulations with different size lattices as leading corrections to the continuum limit are of the order $\mathcal{O}(N_\tau^{-2})$ [23, 24]. Taking the Stefan-Boltzmann result of n_B/T^3 for $N_\tau = 4$ [19], we find as educated guess for the needed continuum extrapolation factor of the net quark number density $d_{lat}^{(n)} = 0.456$. This compares well with continuum extrapolation factors reported in [25, 26], reading 0.446 and 0.465 respectively, where similar actions have been used in the lattice simulations.

In Fig. 1, we compare our model with the continuum estimate of the lattice QCD data [19, 21] for the scaled net quark number density as a function of μ_i/T_c at constant T . Because $n = 3 n_B$ as a function of imaginary chemical potential is found to be purely imaginary, both in Eq. (2) and in the lattice calculations, we exhibit its imaginary part in the following. The parameters of the effective coupling $G^2(T, \mu = 0)$ in Eq. (6) read $T_s = 0.96 T_c$ and $\lambda = 56$ shifting the divergence of $G^2(T, \mu = 0)$ to approximately $T = 0.98 T_c$, where we utilize $T_c = 163$ MeV as given in [16] for the case at hand. Note that we consider only temperatures $T \geq T_c$. The continuum extrapolated lattice QCD data, in particular the pronounced bending of n/T^3 for $T = 1.1 T_c$, are impressively well described by the QPM parametrization. The drastic change in the slope for $T = 1.1 T_c$ signals the onset of the

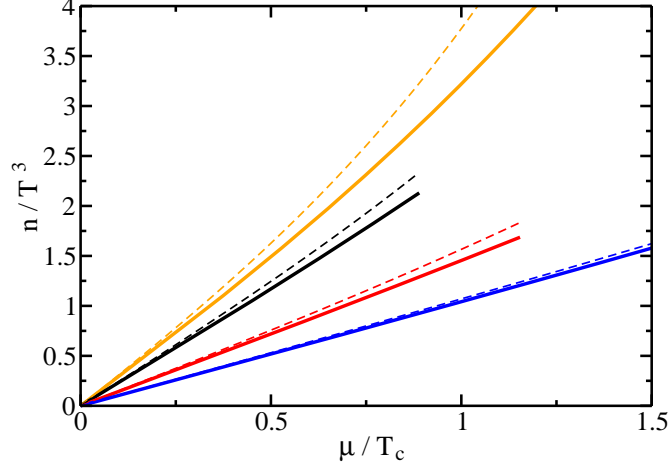


FIG. 2: Continuation of the QPM results for n/T^3 exhibited in Fig. 1 to real chemical potential μ/T_c (solid curves) for $T = 1.1, 1.5, 2.5, 3.5 T_c$ (from top to bottom). For comparison, we also show the analytically continued results (dashed curves) of the polynomial fit from [19] to n/T^3 for imaginary chemical potential.

Roberge-Weiss transition at $\mu_c/T_c = 11\pi/30$, where n should exhibit a discontinuity. In the QPM, this change in slope is driven by the dependence of the quasiparticle asymptotic mass M_∞ on chemical potential and, in particular, by the behavior of G^2 with respect to μ_i as dictated by Peshier's flow equation Eq. (5). We note that n/T^3 exhibited as a function of μ_i/T shows almost no dependence on T for temperatures $T \geq 1.5 T_c$. Below T_c , however, n/T^3 displays a qualitatively different behavior being continuous and periodic as a function of μ_i/T [19].

Within the QPM, results obtained by considering purely imaginary chemical potential can easily be analytically continued to real μ . This is achieved by continuing the purely imaginary variable $\mu = i\mu_i$ to the entire complex plane and finally taking the limit $\text{Im } \mu \rightarrow 0$. In this way, we recover the quasiparticle model [10–12] formulated for real μ . Within the analyticity domain, i. e. for $\mu < \mu_c(T)$, the analytic continuation is unique as guaranteed by general arguments. Keeping the QPM parameters λ and T_s fixed, the results of n/T^3 for real μ/T_c are exhibited in Fig. 2 (solid curves). These results may be compared to other analytic continuations. For instance, in [19], a polynomial fit to n/T^3 as well as its analytic continuation to real μ/T (dashed curves in Fig. 2) was considered. Despite the fact that this polynomial fit $n(T, \mu_i, m_q) = a(T, m_q)\mu_i + b(T, m_q)\mu_i^3$ for imaginary chemical potential, with analytic continuation $n(T, \mu, m_q) = a(T, m_q)\mu - b(T, m_q)\mu^3$, cannot account for the change

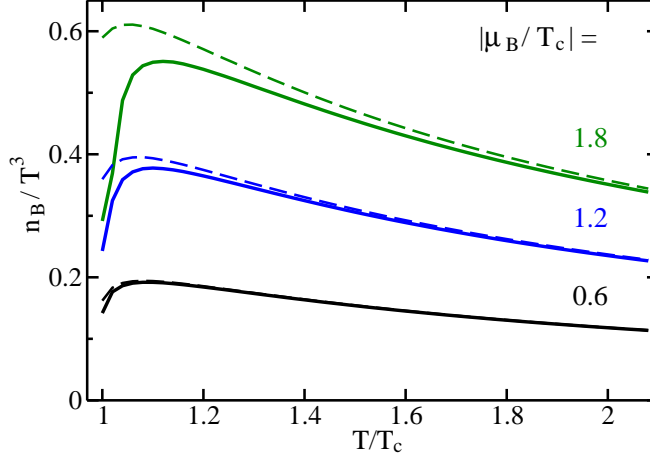


FIG. 3: Scaled net baryon density n_B/T^3 as a function of T/T_c for constant imaginary $\mu_B/T_c = 3i\mu_i/T_c$ (solid curves) and for corresponding real μ_B/T_c (dashed curves). Note that for all temperatures, $\partial n/\partial T > 0$ is fulfilled, as required from thermodynamic stability conditions.

in slope observed for $T = 1.1 T_c$ at large μ_i/T_c , its coefficients a and b are temperature and quark mass dependent. In contrast, the QPM parameters λ and T_s are once adjusted to n/T^3 at $T = 1.1 T_c$ (cf. Fig. 1) and then kept fixed for all temperatures and chemical potentials. In addition, the behavior of analytic continuations of polynomial fits decisively depends on the considered order in μ_i^2 (cf. discussion in [9, 27]). The QPM, in contrast, contains all orders of μ_i^2 respecting the symmetry $\ln Z(\mu) = \ln Z(-\mu)$. As evident from Fig. 2, we point out that close to $\mu_c(T)$ a sensible analytic continuation is needed.

In Fig. 3, the net baryon density n_B/T^3 is exhibited as a function of T/T_c for constant imaginary (solid curves) as well as for real baryo-chemical potential $\mu_B = 3\mu$ (dashed curves). Somewhat surprisingly, the results for real μ_B significantly deviate from the original results for imaginary chemical potential only at large μ_B and temperatures close to T_c . Note that in these considerations μ_B is restricted to $|\mu_B| \leq \pi T$.

Susceptibilities are quantities serving as measures of fluctuations. The quark number susceptibility χ (cf. Eqs. (7, 8)) is simply the derivative of the density in μ_i direction. We exhibit χ/T^2 either at $\mu = 0$ for various temperatures (Fig. 4, left panel) or for $T = 1.1 T_c$ for various values of μ_i (Fig. 4, right panel). Clearly, if lattice QCD data for $n(T, i\mu_i)$ are well described by a model, the model should also describe $\chi(T, i\mu_i)$. This is indeed the case, see Fig. 4, where both, lattice QCD data as well as QPM results, are obtained by numerical differentiation of the net quark number density. The only concern that could arise is that

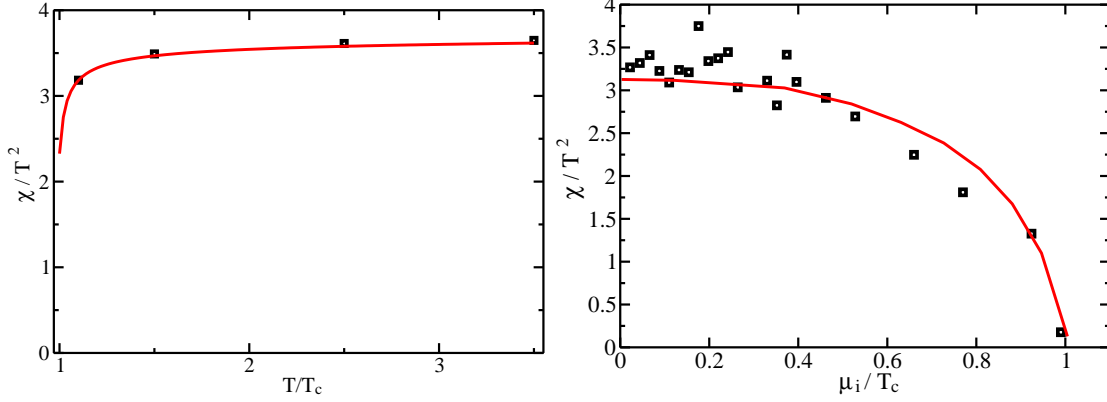


FIG. 4: Left: comparison of the QPM (solid curve) for the scaled quark number susceptibility χ/T^2 as a function of T/T_c for $\mu = 0$ with the continuum estimate of the lattice QCD data in [19] (circles). Right: comparison of the QPM (solid curve) for χ/T^2 as a function of $\mu_i/T_c \leq 1$ for $T = 1.1 T_c$ with the continuum estimate of the lattice QCD data in [21].

derivatives enhance possible systematic differences between a model and the data. Fig. 4 does not point to such a possibility.

B. Deconfinement border line

The solution of Peshier's flow equation Eq. (5) is accomplished by the method of characteristics. As in [11], we consider the characteristic curve emerging at $T = T_c$ and $\mu = 0$ as an indicator of the pseudo-critical line. This transition line has been calculated in lattice simulations [16] for imaginary chemical potential. The lattice QCD data have been analyzed by applying polynomial fits which were analytically continued to real μ [16]. The results of such analytic continuations decisively depend on the chosen degree of the considered polynomial or ratios thereof, as discussed in [9, 27].

In Fig. 5, the phase diagram is exhibited in specific coordinate systems. Negative values $\mu_B^2 \leq 0$ indicate purely imaginary baryo-chemical potential, whereas positive $\mu_B^2 \geq 0$ indicate real μ_B . Diamonds represent the polynomial fit [16] for both, imaginary chemical potential and the corresponding analytically continued results. For comparison, we depict the QPM characteristic (solid) curve starting at $T = T_c$ as solution of Peshier's flow equation Eq. (5) for imaginary chemical potential as well as for real μ_B . The flatness of the curve in the exhibited μ_B^2 interval (left panel) signals the dominance of the μ_B^2 term in agreement with

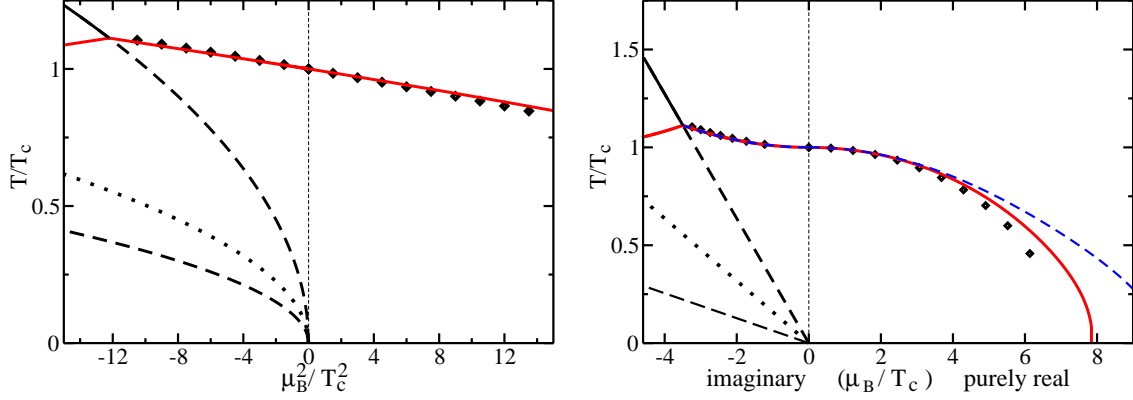


FIG. 5: Phase diagram for imaginary and real baryo-chemical potential. Left: T/T_c vs. μ_B^2/T_c^2 . Right: T/T_c vs. μ_B/T_c . Details are explained in the text.

the polynomial fit findings in [16]. Note, however, that the QPM result contains all orders of μ_B^2 . We emphasize that our model parameters λ and T_s are adjusted to $n(T, i\mu_i)$ at $T = 1.1 T_c$ and have proven above to describe at the same time $n(T, i\mu_i)$ at $T = 1.5, 2.5, 3.5 T_c$. In so far, the agreement of our characteristic curve emerging at T_c with the transition line in [16] is quite satisfying.

In Fig. 5 we also show the first two Roberge-Weiss transition lines (fat dashed curves characterized by [15] $\mu_B^2/T_c^2 = -T^2/T_c^2 \pi^2 (2k+1)^2$ for $k = 1, 2$) at which thermodynamic quantities exhibit an analytic behavior at small temperatures, while the Roberge-Weiss transition represents a first-order phase transition (fat solid section) at sufficiently large T . In addition, the first Z_3 center symmetry line is shown (dotted curve characterized by [15] $\mu_B^2/T_c^2 = -T^2/T_c^2 \pi^2 (2k)^2$ for $k = 1$). The repeated copies of these sectors for $k \geq 2$ are not displayed in Fig. 5; they reside in the left bottom edge.

Numerically, we find that the characteristic curve emerging at $T = T_c$ and the first Roberge-Weiss transition line cross each other at $T^E/T_c = 1.112$ and $(\mu_B^E)^2/T_c^2 = -12.214$, whereas the lattice QCD simulations [16, 19] report $T^E/T_c = 1.095$ and $(\mu_B^E)^2/T_c^2 = -11.834$. These tiny differences can hardly be resolved on the scale displayed in Fig. 5. For larger negative μ_B^2 the characteristic curve is mirrored at the Roberge-Weiss transition line (see the section in the left top edge below the first Roberge-Weiss transition line in the left panel of Fig. 5).

In the right panel of Fig. 5, we exhibit the phase diagram with the same notions as in the left panel, but with a linear abscissa μ_B/T_c ; negative values of μ_B/T_c are to be assigned to

purely imaginary chemical potential, while positive values correspond to purely real values of μ_B . As the coefficients in Peshier's flow equation Eq. (5) for real chemical potential obey $a_T \rightarrow 0$ for $\mu \rightarrow 0$ and $a_\mu \rightarrow 0$ for $T \rightarrow 0$, the characteristic curves, including the one crossing the T axis at T_c , approach the $T = 0$ and $\mu_B = 0$ axes perpendicularly. Deviations between QPM results for real μ_B and the polynomial fit become visible for $\mu_B \geq 330$ MeV. In addition, we exhibit the solution of Peshier's flow equation starting at T_c for a different set of QPM parameters (cf. section IV A) by the dashed line. For imaginary chemical potential, both results are indistinguishable, whereas for real μ deviations become visible for $\mu_B/T_c \geq 2$ signalling again that small deviations in the imaginary chemical potential sector result in larger deviations in the sector of real μ . This makes predictions about the onset of possible deconfinement effects at small T and real μ difficult.

C. Quark mass dependence

In this subsection, we study the influence of a different approximation of the quark dispersion relation on the QPM results. In particular, we concentrate on the characteristic curve emerging at $T = T_c$. Apart from Eq. (3), we can approximate the quark dispersion relation by [28]

$$\omega_q^2 = k^2 + m_q^2 + 2m_q M_+ + 2M_+^2 \quad (9)$$

as for instance employed in [11, 29] with M_+^2 from Eq. (4). Changing the approximation of the dispersion relation ω_q demands a readjustment of the parameters in the effective coupling $G^2(T, \mu = 0)$ in Eq. (6) in order to appropriately describe the lattice QCD data of n/T^3 and causes changes in Peshier's flow equation (see Appendix A). The QPM parameters for using Eq. (9) adjusted to the continuum estimate of the n/T^3 data at $T = 1.1 T_c$ read $T_s = 0.976 T_c$ and $\lambda = 95$ implying that the divergence in $G^2(T, \mu = 0)$ is located at $T = 0.987 T_c$. With this new parametrization, the agreement between QPM and continuum extrapolated lattice QCD data is nearly as perfect as observed in Fig. 1 (at most 3% deviations). However, it indicates that Eq. (3) might be somewhat more suitable than Eq. (9) as quark dispersion relation. The influence on the characteristic curve emerging at $T = T_c$ when employing Eq. (9) instead of Eq. (3) is negligible for imaginary chemical potential. For real μ_B/T_c , the difference between both parametrizations is also very tiny and approximately 1.5% at small temperatures.

In addition, we can discuss the quark mass dependence of the found results by performing a naive chiral extrapolation $m_q \rightarrow 0$. For imaginary chemical potential, quark mass effects turn out to be negligible independent of the specific quark dispersion relation used. For real μ_B/T_c , quark mass effects are also small and visible only for very small temperatures. The differences between using $m_q = 0.2T$ and $m_q = 0$ are less than 1% when employing Eq. (3) and at most 3% when employing Eq. (9). In both cases, decreasing quark masses imply a larger curvature of the characteristic curves and thus a smaller critical chemical potential at $T = 0$. A similar minor quark mass dependence with the same trend when decreasing m_q was found in lattice QCD simulations [30].

Another sensitive measure for the quark mass dependence of the net baryon density n_B is the chemical potential dependence of the chiral condensate $\langle \bar{\psi}\psi \rangle$ which are related to each other by a Maxwell relation [19, 21]. Within the QPM, the μ dependence of $\langle \bar{\psi}\psi \rangle$ is fairly well described and will be reported elsewhere. We note that simply putting $m_q = 0$ but keeping the parametrization of $G^2(T, \mu = 0)$ fixed modifies n/T^3 by less than 1% for the considered range of temperatures and chemical potentials. In principle, however, a general quark mass dependence of the parameters T_s and λ in the effective coupling would be conceivable. Due to the minor effects observed, we restrict our further considerations to quark dispersion relation Eq. (3) in the following.

D. μ dependence of the quasiparticle masses

In [18], the lattice QCD data [31] have been discussed with the goal to extract the relevant excitation modes from thermodynamic bulk quantities. The explicit μ dependence of the quasiparticle masses has been named BKS effect. In order to test the importance of the BKS effect on the found results, we omitted the μ_i^2/π^2 terms in the quasiparticle dispersion relations or flipped their signs though leaving the dependence of G^2 on μ_i unchanged. In fact, neglecting simply the term μ_i^2/π^2 in Eq. (4) (or Eq. (18) below), n/T^3 is only affected for large μ_i , where the attenuation of μ_i^2 by $1/\pi^2$ becomes smaller and the term proportional to μ_i^2 cannot be neglected compared to the term proportional to T^2 . This implies that for larger T significant effects can only be seen at sufficiently large values of μ_i . Note, however, that μ_i is restricted by $\mu_i \leq \frac{\pi}{3}T$. Similar effects can be observed when flipping the signs in the asymptotic mass expressions. Nonetheless, thermodynamic self-consistency of the

QPM requires in both considered cases changes in Peshier's flow equation (5) rendering the coefficients b , a_T and a_{μ_i} according to Maxwell's relation. In such a thermodynamically self-consistent approach, we find our results to be indistinguishable from the QPM results exhibited in Fig. 1, i. e. found results seem to be rather independent of the explicit form of the μ_i dependence in the asymptotic mass expressions. However, a general dependence of the asymptotic masses on the chemical potential seems to be important. When neglecting μ_i completely in the quasiparticle dispersion relations, thermodynamic self-consistency dictates also an independence of T in M_∞ (and m_∞ in Appendix A) which significantly changes the results: even though the almost linear behavior of n/T^3 for small μ_i can be reproduced, the pronounced curvature for $T = 1.1 T_c$ at larger μ_i cannot be obtained under such an assumption. The μ_i dependence of n/T^3 is further discussed in Appendix B.

E. Scaling properties

In [25, 32], a scaling of the ratio $\Delta p/\Delta p^{SB}$ of the excess pressure in μ_B direction was reported. Here, we find a similar scaling for the ratio n_B/n_B^{SB} as depicted in Fig. 6, where n_B^{SB} denotes the Stefan-Boltzmann expression of the net baryon density. When considering

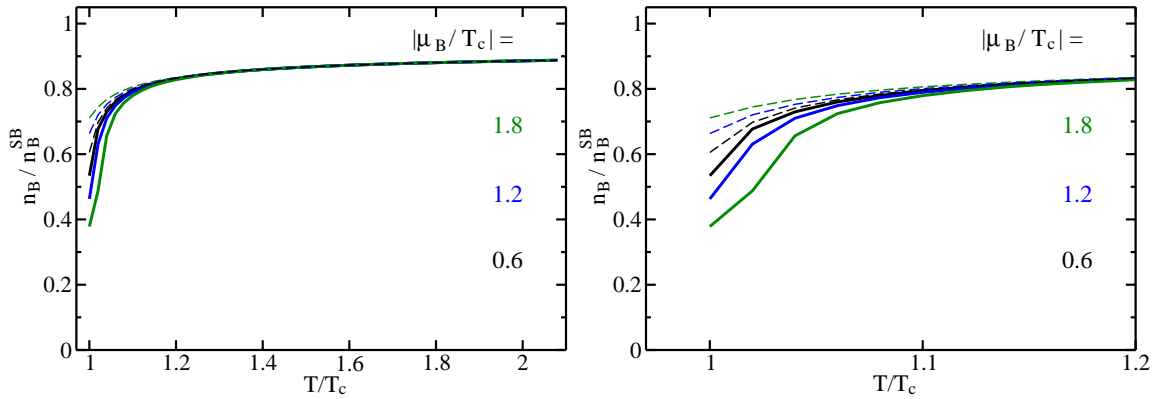


FIG. 6: Left: ratio n_B/n_B^{SB} as a function of T/T_c for different imaginary and real baryo-chemical potentials. Dashed curves represent results for imaginary baryo-chemical potential, with $|\mu_B/T_c| = 0.6, 1.2, 1.8$ from bottom to top, while solid curves depict corresponding results for real μ_B , with $|\mu_B/T_c| = 0.6, 1.2, 1.8$ in inverted order, i. e. from top to bottom. Right: zoom into the region close to T_c .

n_B/n_B^{SB} either for real or for imaginary chemical potential, in both cases, μ_B effects become visible only in the vicinity of T_c . In fact, for the baryo-chemical potentials considered in Fig. 6, the ratio n_B/n_B^{SB} is found to be independent of μ_B for $T \geq 1.2 T_c$. Furthermore, $n_B/n_B^{SB} = 1$ is approached only asymptotically, signalling the expected strong deviations from the free field behavior. Apart from the observed differences in the ratio between real and imaginary chemical potentials close to T_c , we find an interesting pattern: n_B/n_B^{SB} decreases with increasing baryo-chemical potential for real μ_B , while the ratio increases in the case of imaginary chemical potential. This is partly caused by differences in n_B/T^3 between real and imaginary chemical potential which become smaller for increasing temperature (cf. Fig. 3). But it is also related to different signs in n_B^{SB} for real or imaginary chemical potential.

To be specific, in the case of real chemical potential, n_B can be expanded into a Taylor series in powers of μ_B with expansion coefficients [31] $c_k(T) = \frac{1}{k!} \left. \frac{\partial^k (p(T, \mu)/T^4)}{\partial (\mu/T)^k} \right|_{\mu=0}$. The Stefan-Boltzmann expression for the net baryon density reads

$$n_B^{SB}(T, \mu_B) = \frac{N_f}{3} \frac{\mu_B}{3} T^2 + \frac{N_f}{3\pi^2} \left(\frac{\mu_B}{3} \right)^3. \quad (10)$$

Even though this expression for n_B^{SB} is correct only for a massless ideal gas, while n_B entering the ratio is evaluated for $m_q = 0.2 T$, quark mass effects can safely be neglected (as discussed in section III C). The ratio n_B/n_B^{SB} reads

$$\frac{n_B}{n_B^{SB}} \approx \frac{2c_2}{N_f} + \frac{2}{N_f} \left(\frac{\mu_B}{3T} \right)^2 \left[2c_4 - \frac{c_2}{\pi^2} \right] + \mathcal{O}(\mu_B^4). \quad (11)$$

In the limit $\mu_B \rightarrow 0$, the ratio approaches $2c_2/N_f = \frac{1}{4} \chi(T, \mu=0)/T^2$ for $N_f = 4$. For small $\mu_B/(3T)$, i. e. for small μ_B or large T , μ_B effects become small, thus explaining the observed scaling. Furthermore, as $2c_4 - c_2/\pi^2 > 0$ for all temperatures $T \geq T_c$ and remains approximately constant for $T \geq 1.2 T_c$ (cf. section IV B), a fixed ratio n_B/n_B^{SB} requires increasing temperatures T for increasing μ_B , explaining the observed ordering in Fig. 6. Close to T_c , deviations between exact results and the Taylor series expansion of n_B become larger with increasing μ_B , such that the arguments presented here do not apply.

In the case of imaginary chemical potential, $n_B(T, i\mu_i)$ from Eq. (1) can be evaluated for small μ_i by expanding the trigonometric functions in powers of μ_i/T yielding also a Taylor series expansion similar to the one in the sector of real chemical potential. Within this approach, we find

$$n_B(T, i\mu_i) = i \left(\frac{2}{3} \tilde{c}_2 \mu_i T^2 - \frac{4}{3} \tilde{c}_4 \mu_i^3 + \dots \right), \quad (12)$$

where

$$\tilde{c}_k(T) = \frac{1}{k!i^k} \left. \frac{\partial^k (p(T, i\mu_i)/T^4)}{\partial (\mu_i/T)^k} \right|_{\mu_i=0} \equiv c_k(T). \quad (13)$$

Note that both, \tilde{c}_k and c_k are real and $\tilde{c}_k, c_k = 0$ for odd k . The Stefan-Boltzmann result for imaginary chemical potential reads

$$n_B^{SB}(T, i\mu_i) = i \left(\frac{N_f}{3} \mu_i T^2 - \frac{N_f}{3\pi^2} \mu_i^3 \right) \quad (14)$$

and the ratio follows as $\frac{n_B}{n_B^{SB}} \approx \frac{2\tilde{c}_2}{N_f} - \frac{2}{N_f} \left(\frac{\mu_B}{3T} \right)^2 \left[2\tilde{c}_4 - \frac{\tilde{c}_2}{\pi^2} \right] + \mathcal{O}(\mu_B^4)$. Similar to the considerations for real chemical potential, we observe a scaling with $\mu_B/(3T)$ and in the limit $\mu_B \rightarrow 0$, $n_B/n_B^{SB} \rightarrow 2c_2/N_f = \frac{1}{4}\chi(T, \mu=0)/T^2$ for $N_f = 4$. For imaginary chemical potential, however, the sign of the term proportional to μ_B^2 is flipped, explaining the different ordering observed in Fig. 6, i. e. at fixed T , n_B/n_B^{SB} becomes larger with increasing μ_B .

IV. COMPARISON WITH LATTICE QCD DATA AT $\mu = 0$

A. Pressure

Via the QPM, we have access to both, real and imaginary chemical potentials. Thus, we can compare our results based on the lattice QCD data of [19, 21] with other lattice QCD calculations. In [33], a similar lattice setup for calculating the pressure at $\mu = 0$ for $N_f = 4$ degenerate quark flavors with $m_q = 0.2T$ on a lattice with $N_\tau = 4$ and $N_\sigma = 16$ was considered, though employing an improved lattice action. These lattice QCD data [33] require also a proper continuum extrapolation. We apply a similar strategy as in section III A but now for the pressure, because its Stefan-Boltzmann limit is given in [33] for $N_\tau = 4$, and find $d_{lat}^{(p)} = 0.839$ as continuum extrapolation factor. The difference between $d_{lat}^{(p)}$ and $d_{lat}^{(n)}$ in section III is maybe a consequence of the different lattice actions used in the simulations [33] and [19, 21] resulting in different cut-off effects on the data.

In Fig. 7, the continuum estimated lattice QCD data [33] (squares) for p/T^4 as a function of T/T_c at $\mu = 0$ are compared with the QPM using the parameters λ and T_s in $G^2(T, \mu = 0)$ from section III A adjusted to n/T^3 for imaginary chemical potential. The integration constant $B(T_c)$ adjusting the QPM value of p/T^4 at $\mu = 0$ and $T = T_c$ to lattice QCD reads $B(T_c) = 2.56 T_c^4$ using again $T_c = 163$ MeV. As evident from Fig. 7, the general trend of p/T^4 and the behavior at large T is reproduced. Nevertheless, p/T^4 shows deviations of up

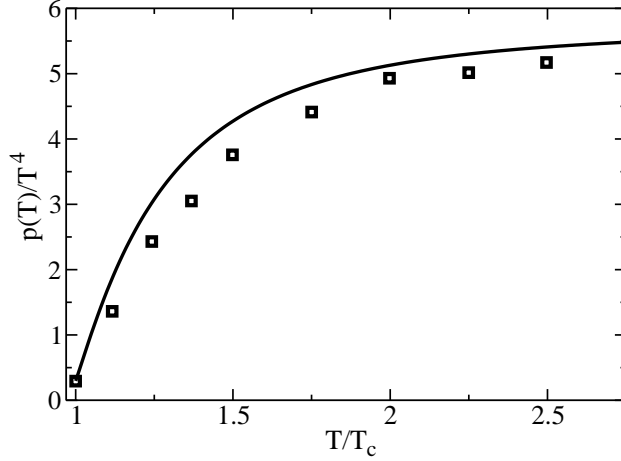


FIG. 7: Comparison of the QPM (solid curve, using parameters as in section III A) for the scaled pressure p/T^4 as a function of T/T_c at $\mu = 0$ with the continuum estimate of the lattice QCD data [33] (squares).

to 20% in the intermediate temperature region $T \sim 1.5 T_c$. The same deviation pattern was already discussed in [14, 25, 29]. In fact, it seems to be a general feature, that fits to lattice QCD data in the sector of zero (non-zero) chemical potential underestimate (overestimate) the according results in the sector of non-zero (zero) chemical potential.

Considering, instead, an independent adjustment of the QPM parameters to p/T^4 at $\mu = 0$, the comparison of the QPM with the continuum estimate of the lattice QCD data is exhibited in Fig. 8 (left panel). We find an impressive agreement when adjusting $T_s = 0.91 T_c$, $\lambda = 16$ and $B(T_c) = 1.25 T_c^4$ with $T_c = 163$ MeV. With this new parametrization, we evaluate the net quark number density for imaginary chemical potential. The results (solid curves) are shown in the right panel of Fig. 8. At constant μ_i/T_c , we find increasing deviations for decreasing temperatures, in particular close to the Roberge-Weiss transition, even though the change in slope close to μ_c is qualitatively still reproduced. Furthermore, using this set of parameters results in the dashed curve in the right panel of Fig. 5 as characteristic curve emerging at $T = T_c$ for real μ_B . With respect to the observed deviations at $T = 1.1 T_c$ between the lattice QCD data from [19, 21] for n/T^3 and the QPM with parameters adjusted to p/T^4 (see right panel of Fig. 8), it is surprising that this characteristic curve agrees so well with the one considered in section III B.

B. Taylor expansion coefficients

Having the QPM parametrizations employed in Figs. 1 and 8 at hand, we can discuss their influence on the Taylor series expansion coefficients $c_k(T)$ defined in section III E for $N_f = 4$ similar to studies for $N_f = 2$ in [14]. In Fig. 9, we exhibit $c_2(T)$ and $c_4(T)$: $c_2(T) = \frac{1}{2}\chi(T, \mu = 0)/T^2$ shows some deviations between both parametrizations whereas $c_4(T)$ agrees fairly well with visible deviations only in the very vicinity of T_c . In addition, we observe that smaller $c_0(T) \equiv p(T, \mu = 0)/T^4$ (cf. Fig. 7 and the left panel of Fig. 8) implies smaller $c_2(T)$ as already pointed out in [29]. As already mentioned in section III A, n/T^3 depicted as a function of μ_i/T shows almost no temperature dependence for $T \geq 1.5 T_c$. This is mainly due to the fact that $c_2(T)$ (upper solid curve in Fig. 9) exhibits also a rather negligible temperature dependence for larger T . Furthermore, $c_4(T)$ is sizeable only close to T_c and approaches its Stefan-Boltzmann limit $1/\pi^2$ for $T \geq 1.2 T_c$. Considering n_B/T^3 in terms of a Taylor series expansion up to order $\mathcal{O}(\mu^3)$, the results for real and imaginary chemical potential differ only in the sign of the cubic term which is $\propto c_4\mu^3$. Thus, the net baryon density evaluated for real or imaginary chemical potential deviates only for larger chemical potentials and close to T_c as evident from Fig. 3. $c_6(T)$ (not exhibited) deviates

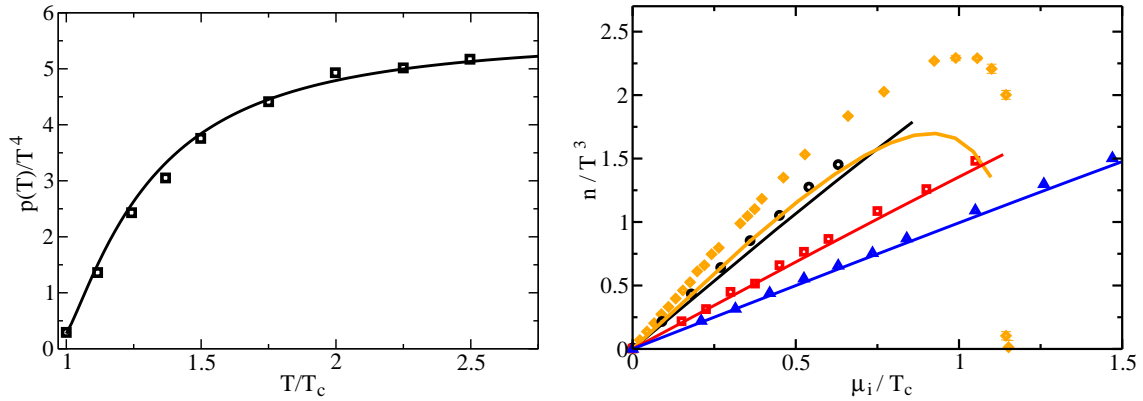


FIG. 8: Left: comparison of the QPM (solid curve) for p/T^4 as a function of T/T_c at $\mu = 0$ employing readjusted parameters (see text) with the continuum extrapolated lattice QCD data (squares) as exhibited in Fig. 7. Right: comparison of the QPM (solid curves, using the readjusted parameters) for n/T^3 as a function of μ_i/T_c for different T with the continuum extrapolated lattice QCD data (symbols) as exhibited in Fig. 1.

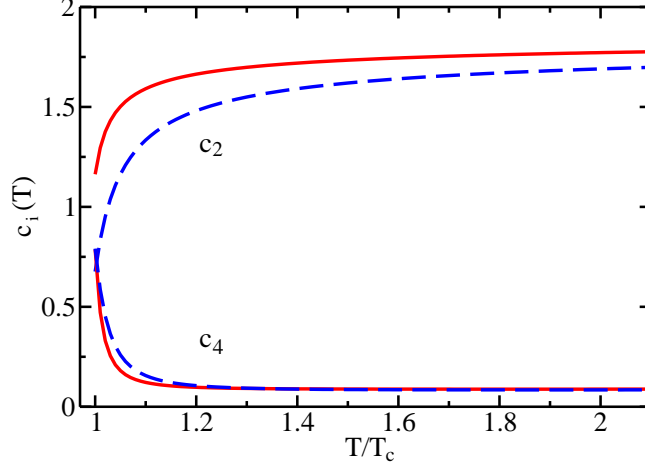


FIG. 9: Taylor series expansion coefficients $c_2(T)$ (upper curves) and $c_4(T)$ (lower curves) as function of T/T_c for $N_f = 4$ employing the different parametrizations from Fig. 1 (solid curves) and Fig. 8 (dashed curves).

significantly from zero only for temperatures very close to T_c but can become of the same order of magnitude as $c_4(T)$ at $T = T_c$.

Finally, we mention that the parametrization in section IV A, optimized for reproducing the $N_f = 4$ lattice QCD data of [33], can also be used to describe the Taylor coefficients

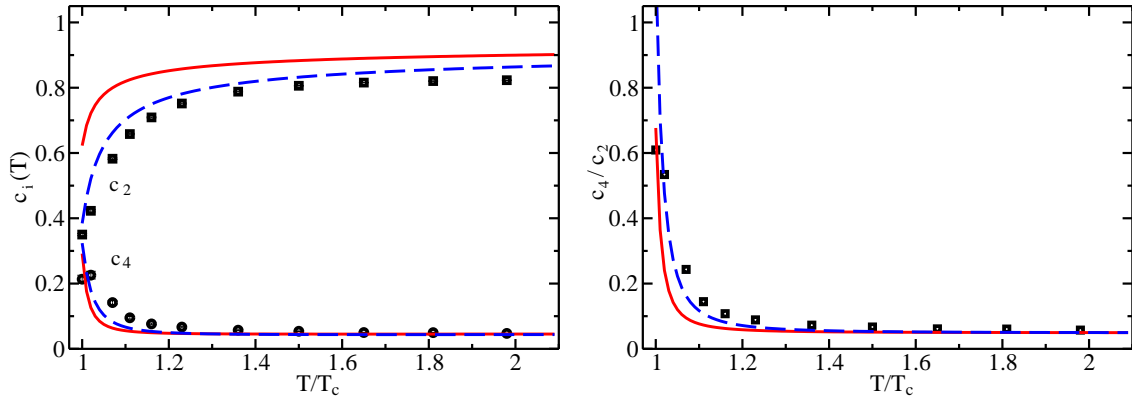


FIG. 10: Left: comparison of lattice QCD data [31] for $N_f = 2$ for $c_2(T)$ (squares) and $c_4(T)$ (circles) as a function of T/T_c with the QPM for $N_f = 2$. Solid curves represent results applying QPM parameters as in Fig. 1 adjusted to n/T^3 while dashed curves represent results applying the parametrization of Fig. 8 adjusted to p/T^4 at $\mu = 0$. Right: ratio c_4/c_2 as a function of T/T_c for both parametrizations.

$c_{2,4}(T)$ from lattice QCD [31] for $N_f = 2$ as exhibited in the left panel of Fig. 10 (dashed curves). In doing so, we keep λ and T_s adjusted to $N_f = 4$ lattice QCD data fixed and change merely from $N_f = 4$ to $N_f = 2$ in the thermodynamic expressions of the QPM. In fact, we find deviations of about 10% close to T_c and less than 5% for $T \geq 1.2 T_c$ between QPM and [31] for $c_2(T)$. While this coincidence might be accidental, one could also argue that the quasiparticle model catches correctly the flavor dependence. In contrast, employing the parametrization from section III A gives a pattern resembling Fig. 9. Even though deviations between both parametrizations are obvious, the ratio c_4/c_2 is rather insensitive with respect to the employed parametrization for $T \geq 1.2 T_c$ approaching $1/(2\pi^2)$ as shown in the right panel of Fig. 10.

V. SUMMARY AND DISCUSSION

In summary we extend our effective quasiparticle model and compare it with lattice QCD data for purely imaginary chemical potential. Despite the fact that our phenomenological model does not exhibit the Roberge-Weiss periodicity of full QCD, it is able to describe the available lattice QCD data [16, 19, 21] impressively well. In particular, the drastic change in slope of n/T^3 close to the critical chemical potential $\mu_c/T = \pi/3$ of the Roberge-Weiss transition can be described. This is entirely due to the BKS effect [18], i. e. a consequence of chemical potential dependent quasiparticle masses. A thermodynamically consistent investigation of the importance of the μ_i dependence in the quasiparticles' asymptotic masses shows that the found results are independent of the chosen explicit form of the μ_i dependence. Nonetheless, the pronounced structures cannot be reproduced when the quasiparticle masses would be completely independent of μ_i . In this respect, the μ_i dependence implemented in the model is confirmed. Another evidence is the comparison of the QPM result for the characteristic curve emerging at $T = T_c$ with the phase transition line evaluated in lattice QCD simulations [16]. For the Roberge-Weiss transition, we find critical values of temperature and baryo-chemical potential close to the ones given in [16]. The successful comparison points to the correctness of Peshier's flow equation as a tool for transporting information from $\mu = 0$ to non-zero μ which is of particular importance for the knowledge of the equation of state at larger baryon densities relevant for CERN-SPS and upcoming FAIR.

With the found QPM parametrization describing lattice QCD data in the sector of purely imaginary chemical potential at hand, we can also compare with an independent set of lattice QCD data [33] obtained at $\mu = 0$. We find some deviations for the pressure in the intermediate temperature region which might account for the different lattice actions used in the calculations but could also signal to some extent a disagreement of results obtained at $\mu = 0$ and non-zero μ , as already discussed in [14, 29]. In this context we emphasize that the comparison of thermodynamic models with lattice QCD data is hampered by the lacking systematic continuum extrapolation of the latter.

Ab initio it is not clear whether the assumed quasiparticle excitations represent the proper description of QCD thermodynamics also in the region close to T_c . The success of the present comparison lends some credibility into the picture of quasiquark excitations with a mass gap. This is in line with findings in [34], where also a striking deviation from the perturbative excitation pattern close to T_c has been found. Nevertheless, it would be premature to claim that the strongly coupled hot quark-gluon medium is entirely described by the presently used quasiparticles. For instance, excitation modes like plasminos and longitudinal gluons are not included in the model. Furthermore, finite width effects of the quasiparticles and Landau damping are neglected. One should keep in mind that thermodynamic bulk properties are sensitive essentially to excitations with hard momenta, i.e. $k \sim T, \mu$. There may be a variety of soft and ultra-hard excitations rendering the picture of the strongly coupled quark gluon plasma into a much more involved scenario, in line with the complexity of QCD.

Our model is far from being an ab initio calculation as attempted in [35]. But, in particular, the flexibility of the introduced effective coupling G^2 allows for curing possible deficits in the dynamical degrees of freedom. Apart from that, the model is highly non-perturbative as it can be formulated in terms of an infinite series of powers in the coupling, though, making contact with perturbation theory, as the first terms coincide with perturbative QCD and asymptotically G^2 approaches the running QCD coupling.

Finally, we remind the reader that we consider here a fairly special case of four degenerate quark flavors. Despite of the known sensitivity of particular features of QCD on the flavor content, some scaling properties of thermodynamic bulk properties may be useful for an orientation in thermodynamic state space.

Acknowledgements

The authors gratefully acknowledge stimulating and enlighting discussions with M. P. Lombardo, as we also thank for supplying lattice QCD data in an early stage of these investigations. Furthermore, we thank P. de Forcrand for interesting conversations. The work is supported by BMBF 06DR136, GSI-FE and EU-I3HP.

Appendix A - Flow equation for imaginary chemical potential

The QPM pressure for imaginary chemical potential reads

$$p(T, i\mu_i) = \sum_{a=q,g} p_a(T, i\mu_i) - B(T, i\mu_i) \quad (15)$$

with partial pressures

$$p_q(T, i\mu_i) = \frac{d_q}{2\pi^2} T \int_0^\infty dk k^2 (\ln [1 + e^{(i\mu_i - \omega_q)/T}] + \ln [1 + e^{(-i\mu_i - \omega_q)/T}]), \quad (16)$$

$$p_g(T, i\mu_i) = -\frac{d_g}{\pi^2} T \int_0^\infty dk k^2 \ln [1 - e^{-\omega_g/T}] \quad (17)$$

for quarks and gluons, respectively, where $d_q = 2N_c N_f$ and $d_g = N_c^2 - 1$. The quasiparticle dispersion relations read $\omega_q^2 = k^2 + m_q^2 + 2M_+^2 \equiv k^2 + M_\infty^2$ with M_+^2 given in Eq. (4) and $\omega_g^2 = k^2 + m_\infty^2$ with asymptotic mass

$$m_\infty^2 = \frac{1}{12} \left([2N_c + N_f] T^2 - \frac{N_c}{\pi^2} N_f \mu_i^2 \right) G^2(T, i\mu_i). \quad (18)$$

Assuming that all T and μ_i dependence of the function B is encoded in the asymptotic mass expressions M_∞ and m_∞ , thermodynamic consistency is fulfilled from the stationarity conditions $\partial p / \partial M_\infty^2 = \partial B / \partial M_\infty^2$ and $\partial p / \partial m_\infty^2 = \partial B / \partial m_\infty^2$ [36] such that entropy density s and net quark number density n are obtained from standard thermodynamic relations. The purely real result for $s = s_q + s_g$ reads

$$s_q(T, i\mu_i) = \frac{d_q}{2\pi^2 T} \int_0^\infty dk k^2 \left(\frac{\frac{4}{3}k^2 + M_\infty^2}{\omega_q} [f_q^+ + f_q^-] - i\mu_i [f_q^+ - f_q^-] \right), \quad (19)$$

$$s_g(T, i\mu_i) = \frac{d_g}{\pi^2 T} \int_0^\infty dk k^2 \frac{\frac{4}{3}k^2 + m_\infty^2}{\omega_g} \frac{1}{e^{\omega_g/T} - 1}, \quad (20)$$

where $f_q^\pm = (e^{(\omega_q \mp i\mu_i)/T} + 1)^{-1}$ and n is given in Eq. (1). The quasi-linear partial differential equation Eq. (5) to be solved for $G^2(T, i\mu_i)$ follows from Maxwell's relation

$$\frac{\partial s}{\partial(i\mu_i)} = \frac{\partial^2 p}{\partial(i\mu_i)\partial T} = \frac{\partial^2 p}{\partial T \partial(i\mu_i)} = \frac{\partial n}{\partial T}, \quad (21)$$

where the explicit derivative terms cancel each other leaving

$$\frac{\partial n}{\partial M_\infty^2} \frac{\partial M_\infty^2}{\partial T} = \frac{\partial s_q}{\partial M_\infty^2} \frac{\partial M_\infty^2}{\partial(i\mu_i)} + \frac{\partial s_g}{\partial m_\infty^2} \frac{\partial m_\infty^2}{\partial(i\mu_i)}. \quad (22)$$

Omitting the overall factor of i in $\partial n/\partial M_\infty^2$, $\partial M_\infty^2/\partial(i\mu_i)$ and $\partial m_\infty^2/\partial(i\mu_i)$, the coefficients of Eq. (5) read

$$b = \left(\frac{C_f}{2} T G^2 + 2m_q a \right) I_1 - \frac{N_c N_f}{6\pi^2} \mu_i G^2 I_2 - \frac{C_f}{2\pi^2} \mu_i G^2 I_3, \quad (23)$$

$$a_T = -\frac{C_f}{4} \left(T^2 - \frac{\mu_i^2}{\pi^2} \right) I_1, \quad (24)$$

$$a_{\mu_i} = -\frac{1}{12} \left([2N_c + N_f] T^2 - \frac{N_c N_f}{\pi^2} \mu_i^2 \right) I_2 - \frac{C_f}{4} \left(T^2 - \frac{\mu_i^2}{\pi^2} \right) I_3, \quad (25)$$

where $C_f = (N_c^2 - 1)/(2N_c)$ and the integral expressions explicitly read

$$I_1 = \frac{d_q}{2\pi^2 T} \int_0^\infty dk \frac{k^2}{\omega_q} \frac{(e^{\omega_q/T} \sin(\mu_i/T) - e^{3\omega_q/T} \sin(\mu_i/T))}{(e^{2\omega_q/T} + 2e^{\omega_q/T} \cos(\mu_i/T) + 1)^2}, \quad (26)$$

$$I_2 = \frac{d_g}{\pi^2 T} \int_0^\infty dk \frac{k^2}{\omega_g} \frac{1}{(e^{\omega_g/T} - 1)} \left(1 - \frac{(\frac{4}{3}k^2 + m_\infty^2)}{2\omega_g^2} \left[1 + \frac{\omega_g}{T} \frac{e^{\omega_g/T}}{(e^{\omega_g/T} - 1)} \right] \right), \quad (27)$$

$$I_3 = \frac{d_q}{2\pi^2 T} \int_0^\infty dk \frac{k^2}{\omega_q} \left(\frac{2e^{\omega_q/T} \cos(\mu_i/T) + 2}{e^{2\omega_q/T} + 2e^{\omega_q/T} \cos(\mu_i/T) + 1} \left[1 - \frac{(\frac{4}{3}k^2 + M_\infty^2)}{2\omega_q^2} \right] \right. \\ \left. - \frac{(\frac{4}{3}k^2 + M_\infty^2)}{2\omega_q T} \frac{(2e^{3\omega_q/T} \cos(\mu_i/T) + 4e^{2\omega_q/T} + 2e^{\omega_q/T} \cos(\mu_i/T))}{(e^{2\omega_q/T} + 2e^{\omega_q/T} \cos(\mu_i/T) + 1)^2} \right. \\ \left. + \frac{\mu_i}{T} \frac{(e^{\omega_q/T} \sin(\mu_i/T) - e^{3\omega_q/T} \sin(\mu_i/T))}{(e^{2\omega_q/T} + 2e^{\omega_q/T} \cos(\mu_i/T) + 1)^2} \right). \quad (28)$$

The term in b proportional to a stems from assuming temperature dependent quark masses $m_q = aT$ as employed in some lattice QCD performances, e. g. [19, 21, 31, 33, 37].

The quark number susceptibility χ in Eq. (7) is found to be symmetric when replacing μ_i by $-\mu_i$ because the same holds true for $\partial G^2/\partial\mu_i$. From Eq. (5) we find

$$\frac{\partial G^2}{\partial\mu_i} = \frac{b}{a_{\mu_i}} - \frac{a_T}{a_{\mu_i}} \frac{\partial G^2}{\partial T}. \quad (29)$$

For the individual expressions entering Eq. (29) we find $I_1 \rightarrow -I_1$, $I_2 \rightarrow I_2$ and $I_3 \rightarrow I_3$ for $\mu_i \rightarrow -\mu_i$ such that $b \rightarrow -b$, $a_T \rightarrow -a_T$ and $a_{\mu_i} \rightarrow a_{\mu_i}$. In addition, a Taylor series expansion of $G^2(T, i\mu_i)$ in powers of μ_i consists only of even powers in μ_i [13, 14] such that $\partial G^2/\partial T$ is symmetric under $\mu_i \rightarrow -\mu_i$. In the limit $\mu_i \rightarrow 0$, we find $\partial G^2/\partial\mu_i \rightarrow 0$ as $b \rightarrow 0$, $a_T \rightarrow 0$ but a_{μ_i} and $\partial G^2/\partial T$ remain non-zero.

When employing the quark dispersion relation Eq. (9), the coefficients of the flow equation render to

$$b = \left[\left(\frac{C_f}{4} + m_q \sqrt{\frac{C_f}{8 \left(T^2 - \frac{\mu_i^2}{\pi^2} \right) G^2}} \right) 2TG^2 + 2m_q a + 2aM_+ \right] I_1 - \frac{N_c N_f}{6\pi^2} \mu_i G^2 I_2 - 2 \frac{\mu_i}{\pi^2} G^2 \left(\frac{C_f}{4} + m_q \sqrt{\frac{C_f}{8 \left(T^2 - \frac{\mu_i^2}{\pi^2} \right) G^2}} \right) I_3, \quad (30)$$

$$a_T = - \left(T^2 - \frac{\mu_i^2}{\pi^2} \right) \left(\frac{C_f}{4} + m_q \sqrt{\frac{C_f}{8 \left(T^2 - \frac{\mu_i^2}{\pi^2} \right) G^2}} \right) I_1, \quad (31)$$

$$a_{\mu_i} = -\frac{1}{12} \left([2N_c + N_f] T^2 - \frac{N_c N_f}{\pi^2} \mu_i^2 \right) I_2 - \left(T^2 - \frac{\mu_i^2}{\pi^2} \right) \left(\frac{C_f}{4} + m_q \sqrt{\frac{C_f}{8 \left(T^2 - \frac{\mu_i^2}{\pi^2} \right) G^2}} \right) I_3. \quad (32)$$

Appendix B - Parametrizing the μ_i dependence

In section III, we found a general dependence of the quasiparticle dispersion relations on temperature and chemical potential to be of utmost importance for the successful description of lattice QCD data. This shall be illustrated in some more detail by considering the net quark number density in Eq. (1) of an ideal gas with dispersion relation $\omega_q^2 = k^2 + M^2$. In principle, thermodynamic self-consistency demands either a dependence of M on both, T and μ_i , or neither a T nor a μ_i dependence of M . In the latter case of constant M , we adjust $M = 0.21$ GeV in order to describe the continuum extrapolated lattice QCD data of n/T^3 (cf. Fig. 1) at $T = 1.1 T_c$ for small μ_i/T_c . The corresponding QPM results for $T = 1.1, 1.5, 2.5, 3.5 T_c$ are then exhibited in the left panel of Fig. 11 (dashed curves). At $T = 1.1 T_c$, we find increasing deviations from the lattice QCD data for $\mu_i/T_c > 0.66$, in particular in the vicinity of the Roberge-Weiss critical chemical potential μ_c , where the pronounced curvature cannot be reproduced. This was already discussed in [21] by considering the ratio $n(\mu_i)/n(\mu_i)_{free}$ signalling clear deviations of the lattice QCD data from a free (ideal) gas behavior. Furthermore, by increasing T but keeping M fixed, the description of the lattice QCD data becomes less and less accurate for smaller μ_i/T_c suggesting a general dependence of M on T . Readjusting M individually for each temperature, ignoring for the moment being

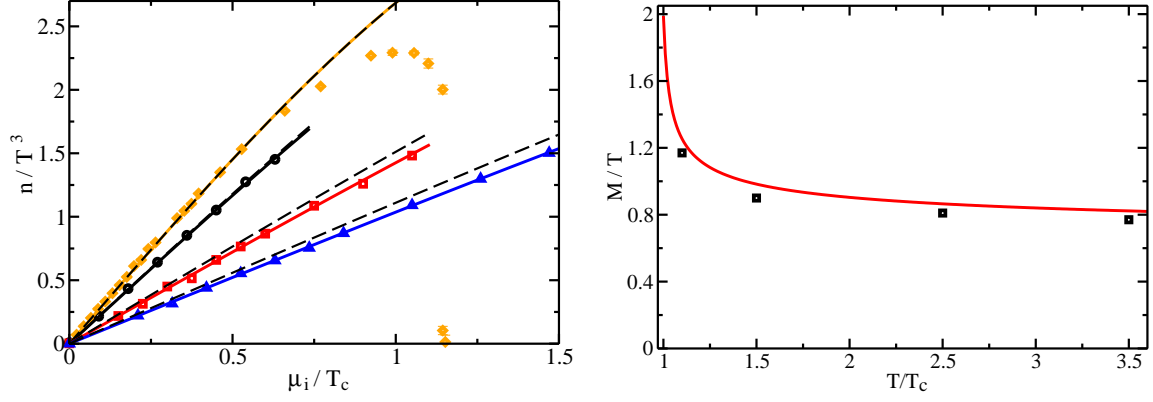


FIG. 11: Left: comparison of ideal gas results for n/T^3 as a function of μ_i/T_c employing either a constant mass parameter $M = 0.21$ GeV (dashed curves) or readjusting $M/T = 1.17, 0.90, 0.81, 0.77$ for $T = 1.1, 1.5, 2.5, 3.5 T_c$ (solid curves from top to bottom) with the continuum extrapolated lattice QCD data (symbols) as exhibited in Fig. 1. Right: comparison of found M/T (squares) as a function of T/T_c with the asymptotic quark mass M_∞/T of the QPM at $\mu = 0$ employing $T_s = 0.96 T_c$ and $\lambda = 56$ as in section III A.

thermodynamic self-consistency, the results are depicted by solid curves in the left panel of Fig. 11. The found scaled mass parameters M/T for the temperatures considered here are exhibited in the right panel of Fig. 11 (squares) and compared with the scaled asymptotic quark mass M_∞/T of the QPM at $\mu = 0$ (solid curve) employing the parametrization of section III A. Both results agree fairly well, indicating that non-zero chemical potential effects are tiny for small μ_i/T but become sizeable close to $\mu_c(T)$ as also visualized in Fig. 12. In Fig. 12, the scaled asymptotic quark mass M_∞/T of the QPM is exhibited as a function of μ_i/T_c for constant T using the QPM parametrization of section III A perfectly describing n/T^3 in Fig. 1. For increasing T , M_∞/T shows decreasing sensitivity on μ_i while non-zero chemical potential effects become important close to $\mu_c = \frac{\pi}{3}T$.

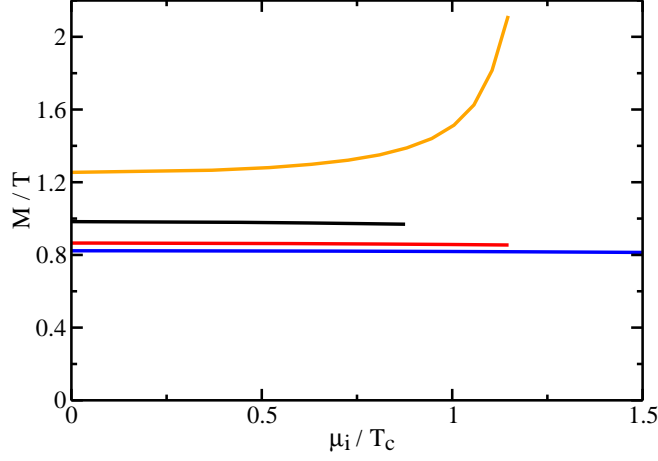


FIG. 12: Asymptotic quark mass M_∞/T of the QPM (solid curves) as a function of μ_i/T_c for $T = 1.1, 1.5, 2.5, 3.5 T_c$ (from top to bottom) employing the QPM parameters from section III A.

-
- [1] F. Karsch, Lect. Notes Phys. **583**, 209 (2002).
 - [2] T. Hatsuda, Invited Talk given at the Workshop on the Physics of High Baryon Density, December 15-16, 2005, GSI, Darmstadt, Germany; T. Hatsuda, and T. Kunihiro, Phys. Rev. Lett. **55**, 158 (1985).
 - [3] Proceedings of Critical Point and Onset of Deconfinement - 3rd International Workshop, July 3-6, 2006, Florence, Italy, (Ed.) F. Becattini; 4th International Workshop, July 9-13, 2007, Darmstadt, Germany, (Eds.) P. Senger et al..
 - [4] M. Gyulassy, and L. McLerran, Nucl. Phys. A **750**, 30 (2005).
 - [5] D. A. Teaney, Phys. Rev. C **68**, 034913 (2003); J. Phys. G **30**, S1247 (2004); Nucl. Phys. A **785**, 44 (2007).
 - [6] E. V. Shuryak, and I. Zahed, Phys. Rev. D **70**, 054507 (2004); E. V. Shuryak, Nucl. Phys. A **750**, 64 (2005); A. Peshier, and W. Cassing, Phys. Rev. Lett. **94**, 172301 (2005).
 - [7] E. Laermann, and O. Philipsen, Ann. Phys. Nucl. Part. Sci. **53**, 163 (2003).
 - [8] O. Philipsen, PoS **LAT2005**, 016 (2006); PoS **JHW2005**, 012 (2006).
 - [9] C. Schmidt, PoS **LAT 2006**, 021 (2006).
 - [10] A. Peshier, B. Kämpfer, O. P. Pavlenko, and G. Soff, Phys. Lett. B **337**, 235 (1994); Phys. Rev. D **54**, 2399 (1996).

- [11] A. Peshier, B. Kämpfer, and G. Soff, Phys. Rev. C **61**, 045203 (2000); Phys. Rev. D **66**, 094003 (2002).
- [12] M. Bluhm, B. Kämpfer, R. Schulze, and D. Seipt, Eur. Phys. J. C **49**, 205 (2007).
- [13] M. Bluhm, Diploma Thesis, Technische Universität Dresden, August 2004.
- [14] M. Bluhm, B. Kämpfer, and G. Soff, Phys. Lett. B **620**, 131 (2005).
- [15] A. Roberge, and N. Weiss, Nucl. Phys. B **275**, 734 (1986).
- [16] M. D’Elia, and M.-P. Lombardo, Phys. Rev. D **67**, 014505 (2003).
- [17] D. Seipt, Diploma Thesis, Technische Universität Dresden, May 2007.
- [18] J. Liao, and E. V. Shuryak, Phys. Rev. D **73**, 014509 (2006).
- [19] M. D’Elia, and M.-P. Lombardo, Phys. Rev. D **70**, 074509 (2004).
- [20] M.-P. Lombardo, Prog. Theor. Phys. Suppl. **153**, 26 (2004); M. D’Elia, F. Di Renzo, and M.-P. Lombardo, AIP Conf. Proc. **806**, 245 (2006).
- [21] M. D’Elia, F. Di Renzo, and M.-P. Lombardo, [[arXiv:0705.3814 \[hep-lat\]](#)].
- [22] M.-P. Lombardo, Prog. Theor. Phys. Suppl. **153**, 26 (2004).
- [23] G. Boyd, J. Engels, F. Karsch, E. Laermann, C. Legeland, M. Lütgemeier, and B. Petersson, Nucl. Phys. B **469**, 419 (1996).
- [24] F. Karsch, Lect. Notes Phys. **583**, 209 (2002).
- [25] K. K. Szabo, and A. I. Toth, J. High Energy Phys. **06**, 008 (2003).
- [26] R. V. Gavai, and S. Gupta, Phys. Rev. D **67**, 034501 (2003); (private communication, March 2006).
- [27] M.-P. Lombardo, PoS **CPOD2006**, 003 (2006).
- [28] R. D. Pisarski, Nucl. Phys. A **498**, 423c (1989); A. Peshier, TFT’98 Proceedings, hep-ph/9809379.
- [29] M. Bluhm, B. Kämpfer, R. Schulze, D. Seipt, and U. Heinz, Phys. Rev. C **76**, 034901 (2007).
- [30] C. R. Allton, S. Ejiri, S. J. Hands, O. Kaczmarek, F. Karsch, E. Laermann, C. Schmidt, and L. Scorzato, Phys. Rev. D **66**, 074507 (2002).
- [31] C. R. Allton, S. Ejiri, S. J. Hands, O. Kaczmarek, F. Karsch, E. Laermann, and C. Schmidt, Phys. Rev. D **68**, 014507 (2003); C. R. Allton, M. Döring, S. Ejiri, S. J. Hands, O. Kaczmarek, F. Karsch, E. Laermann, and K. Redlich, Phys. Rev. D **71**, 054508 (2005).
- [32] Z. Fodor, S. D. Katz, and K. K. Szabo, Phys. Lett. B **568**, 73 (2003); F. Csikor, G. I. Egri, Z. Fodor, S. D. Katz, K. K. Szabo, and A. I. Toth, Nucl. Phys. Proc. Suppl. **119**, 547 (2003).

- [33] J. Engels, R. Joswig, F. Karsch, E. Laermann, M. Lütgemeier, and B. Petersson, Phys. Lett. B **396**, 210 (1997).
- [34] F. Karsch, and M. Kitazawa, [arXiv:0708.0299 [hep-lat]].
- [35] J. P. Blaizot, E. Iancu, and A. Rebhan, Phys. Rev. Lett. **83**, 2906 (1999); Phys. Lett. B **470**, 181 (1999); Phys. Rev. D **63**, 065003 (2001); Phys. Lett. B **523**, 143 (2001); Phys. Rev. D **68**, 025011 (2003); and in *Quark Gluon Plasma 3*, edited by R. C. Hwa and X. N. Wang (World Scientific, Singapore, 2004), p. 60.
- [36] M. I. Gorenstein, and S. N. Yang, Phys. Rev. D **52**, 5206 (1995).
- [37] F. Karsch, E. Laermann, and A. Peikert, Phys. Lett. B **478**, 447 (2000).